1   **High-content assay for CFTR monitoring: simultaneous quantification of channel**

2   **function and biogenesis.**

3   Stella Prins[1], Emily Langron[1], Cato Hastings[2], Emily J. Hill[1], Andra C. Stefan[3], Lewis D.

4   Griffin[2] and Paola Vergani[1]*

5

6   [1] Department of Neuroscience, Physiology and Pharmacology

7   [2] CoMPLEX

8   [3] Natural Sciences

9

10   University College London

11   Gower Street

12   WC1E 6BT London UK

13

14   The first two authors contributed equally to this project.

15   *Correspondence to: p.vergani@ucl.ac.uk

16

17   Running title: Simultaneous screening of CFTR biogenesis and function

Summary

CFTR mutations cause cystic fibrosis by affecting how many channels reach the membrane, and/or how well they work. This study presents an assay that simultaneously measures CFTR biogenesis and function. A screen of 62 disease-causing mutations provides clues on how approved drug VX-770 works.

Abstract

Cystic fibrosis (CF) is a life-limiting disease caused by mutations in the *CFTR* gene, encoding a plasma membrane anion-selective channel. Because CF-causing mutations affect both CFTR permeation/gating and biogenesis, multi-assay approaches have been implemented in drug development, sequentially screening for channel function and membrane density. Here we present the first assay capable of simultaneous assessment of both CFTR characteristics.

To validate our assay, we investigate F508del-CFTR, the most common disease-causing mutant, confirming rescue by incubation at low temperature, treatment with CFTR-targeting drugs and introduction of second-site revertant mutation R1070W. In addition, we characterize a panel of 62 CF-causing mutations and profile effects of acute treatment with approved drug VX-770 (ivacaftor). Measurements using the rare mutation panel correlate well with published results, further validating the assay. Furthermore, mapping the potentiation profile on CFTR structures raises mechanistic hypotheses on drug action, suggesting that VX-770 might allow an open-channel conformation with an alternative arrangement of domain interfaces around site 1.

The assay is a powerful tool for investigation of CFTR ion channel biophysics, allowing rapid and accurate inferences on gating/permeation properties and on how these are affected by mutations and compounds. By providing a two-dimensional molecular characterization of mutant CFTR proteins, our assay can better inform development of therapies tailored for individual CFTR variants. Finally, the integrated assay boosts the potential for discovery of dual-acting compounds, simultaneously repairing both biogenesis and function.

Keywords: protein transport, fluorescence imaging, precision medicine, VX-770.

47 **Non-standard Abbreviations**

48 ABC ATP-binding cassette

49 CF Cystic Fibrosis

50 CFTR Cystic Fibrosis Transmembrane Conductance Regulator

51 $F_{\text{mCherry cell}}$ average normalized mCherry fluorescence intensity over the entire cell

52 $F_{\text{YFP cell}}$ average normalized YFP fluorescence intensity over the entire cell

53 $F_{\text{YFP membrane}}$ average normalized YFP fluorescence intensity within the membrane zone

54 G_{CFTR} CFTR conductance

55 G_{trans} transient anion conductance

56 IRES internal ribosome entry site

57 NBD nucleotide binding domain

58 PDL poly-D-lysine

59 P_{O} open probability

60 ρ CFTR membrane density, as defined in this paper

61 SSR sum of squared residuals

62 τ_{trans} time constant of the transient anion conductance

63 TM transmembrane helix

64 V_{M} membrane potential

65 WT wild type

66 YFP yellow fluorescent protein

Introduction

Cystic fibrosis (CF) is a common life-limiting genetic disease. Although the median survival age has increased by almost 12 years over the last decade, the disease still strongly impacts expectation and quality of life (Elborn, 2016).

CF is caused by mutations in the *CFTR* gene (Riordan et al., 1989; Rommens et al., 1989), encoding an anion-selective channel (Csanády et al., 2019) present on the apical plasma membrane of epithelial cells. These mutations decrease the density of CFTR channels located on the cell membrane (by affecting protein synthesis, folding, intracellular trafficking, plasma membrane stability), and/or impair channel function (impacting on gating or anion permeation). As a result, transepithelial fluid movement is abnormal, creating problems particularly affecting lungs, pancreas, intestines, liver and reproductive systems.

Engineering of a halide sensitive YFP with increased affinity for iodide and a low affinity for chloride (Galietta et al., 2001a; Galietta et al., 2001b), allowed the first high throughput screening projects, which assessed CFTR activity by measuring the rate of YFP quenching caused by iodide influx and chloride efflux (Ma et al., 2002; Pedemonte et al., 2005a; Pedemonte et al., 2005b; Yang et al., 2003). Later, Vertex Pharmaceuticals used changes in membrane potential, monitored through fluorescence resonance energy transfer, to indirectly quantify CFTR channel function (Van Goor et al., 2009; Van Goor et al., 2006).

These efforts led to the identification of the first CFTR modulator drugs, directly targeting the defective CFTR protein. Modulators have been classified as either "potentiators", increasing CFTR channel function, or "correctors" increasing the number of CFTR channels on the plasma membrane. The potentiator ivacaftor (VX-770, Vertex Pharmaceuticals) (Van Goor et al., 2009) is now approved for the treatment of patients carrying the G551D gating mutation and a number of other mutations impairing channel function (Gentzsch and Mall, 2018). However, neither potentiation by VX-770 on its own (Flume et al., 2012), nor treatment with the corrector, VX-809 (Van Goor et al., 2011), alone (Clancy et al., 2012), significantly improves lung function of patients homozygous for the F508del mutation, present on at least one allele in ~90% of patients. Like many other CF-causing mutations, F508del results not only in ion channel dysfunction, but also in a reduction of the number of channels present at the cell surface. Combination treatment with VX-770 and VX-809 provides small but significant health benefits (Wainwright et al., 2015). Triple combination therapies, combining two different correctors with a potentiator, hold promise to further improve patient outcomes (Davies et al., 2018; Keating et al., 2018).

4

100   More than 300 CF-causing mutations have been characterized (The Clinical and

101   Functional TRanslation of CFTR (CFTR2); available at http://cftr2.org). Each mutation, other

102   than F508del, is extremely rare, and is likely to affect the folding, trafficking, stability, gating

103   dynamics and/or permeation of the encoded CFTR protein differently. Pre-clinical data

104   informing on how mutations and drugs affect individual CFTR variants in controlled, *in vitro*

105   systems, is thus very valuable for drug development and trial design.

106   Here we present a medium-throughput image-based assay that acquires multi-

107   dimensional data (dual-colour fluorescence intensity in time and space) on individual live

108   HEK293 cells and extracts information on two key characteristics of CFTR. By co-expressing

109   soluble mCherry with the halide sensitive YFP (Galietta et al., 2001a) linked to CFTR (Langron

110   et al., 2017), our new assay gives readouts of both CFTR function, and CFTR membrane

111   density. Experimental manipulation - incubation at low temperature (Denning et al., 1992;

112   Rennolds et al., 2008; Wang et al., 2008), treatment with VX-809 (He et al., 2013; Okiyoneda

113   et al., 2013) with and without VX-770 (Cholon et al., 2014; Veit et al., 2014), and addition of

114   revertant mutation R1070W (Farinha et al., 2013; Okiyoneda et al., 2013; Thibodeau et al.,

115   2010) - results in the expected changes in measured F508del-CFTR channel function and

116   membrane density. Finally, we present a screening platform suitable for quantifying the

117   molecular characteristics of 62 CFTR variants carried by CF patients, and profile the effects of

118   VX-770 on this panel. Our results validate the assay as a valuable tool for investigation of

119   CFTR molecular mechanism and pharmacology.

120

121

122   **Materials and methods**

123   *Construction of the pIRES2-mCherry-YFPCFTR plasmid*

124   The pIRES2-mCherry-YFPCFTR plasmid was obtained with two sequential

125   subcloning steps. First, a 1.727kb region of pcDNA3.1-YFP-CFTR (Langron et al., 2017),

126   containing the YFP-coding sequence, was subcloned into pIRES-eGFP-CFTR, a gift from

127   David Gadsby (Rockefeller University), using the NheI and BlpI restriction sites. Subsequently

128   a 0.737 kb region from pIRES2-mCherry-p53 deltaN (Lin et al., 2013) (Addgene), containing

129   the mCherry-coding segment and part of the IRES, was subcloned into the pIRES-eGFP-

130   YFPCFTR plasmid using the NotI and BmgBI/BtrI restriction sites. This resulted in the

131   pIRES2-mCherry-YFPCFTR plasmid, with the IRES2 positioned between the two open

132   reading frames for mCherry and YFP-CFTR.

133

HEK293 cell culture, transfection and incubation

HEK293 cells were maintained in Dulbecco's modified Eagle's medium (DMEM), supplemented with 2 mM L-glutamine, 100 U/ml penicillin and streptomycin, and 10% fetal bovine serum (all Life Technologies). Cells were seeded in poly-D-lysine-coated, black-walled 96-well plates (Costar, Fisher Scientific), and transiently transfected with the pIRES2-mCherry-YFPCFTR plasmid using Lipofectamine 2000 (Life Technologies). After transfection, cell plates were returned to the 37°C incubator for 24 hours. Prior to imaging plates were incubated for another 24 hours, at 37°C or 28°C, in 100 µl DMEM including DMSO (vehicle), 10 µM VX-809, or 10 µM VX-770 plus 10 µM VX-809 (Selleck Chemicals).

Image acquisition

Before imaging, cells were washed twice with 100 µL standard buffer (140 mM NaCl, 4.7 mM KCl, 1.2 mM $MgCl_2$, 5 mM HEPES, 2.5 mM $CaCl_2$,1mM glucose, pH 7.4). The ImageXpress Micro XLS (Molecular Devices), an automated inverted wide-field fluorescence microscope with a temperature-controlled chamber (set to 37°C or 28°C, as indicated), was used for image acquisition. Protocols for automated fluid additions, enabled by a robotic arm, were created using MetaXpress software (Molecular Devices). For imaging of YFP(H148Q/I152L)-CFTR, a 472 ± 30 nm excitation filter, and a 520 ± 35 nm emission filter were used. Excitation/emission filters at 531 ± 20 nm and 592 ± 20 nm were used for imaging of mCherry.

For localization of CFTR, a 60× objective was used to take 9 16-bit images per well of both fluorophores. To evaluate CFTR function, a 20× objective was used. Two 16-bit images of mCherry were taken, one at the start and one the end of the protocol. In addition, 16-bit images of the YFP fluorescence, were taken at an acquisition frequency of 0.5 Hz. For the I⁻ first protocol ((A), see below), after 20 s, 50 µl of 300 mM I⁻ buffer (300 mM NaI, 4.7 mM KCl, 1.2 mM $MgCl_2$, 5 mM HEPES, 2.5 mM $CaCl_2$,1mM glucose, pH 7.4) was added to the standard buffer, so that the final concentration of I⁻ in the extracellular medium was 100 mM. Another 40 s later, a further 50 µl of a 100 mM I⁻ buffer containing 40 µM forskolin (100 mM NaI, 4.7 mM KCl, 1.2 mM $MgCl_2$, 5 mM HEPES, 2.5 mM $CaCl_2$,1mM glucose, 40 µM forskolin, pH 7.4) was added, so that the final concentration of forskolin in the extracellular medium was 10 µM, while concentration of I⁻ and other components remained unaltered. For the I- last protocol ((B), below), after 20 s of imaging, CFTR was activated, in the absence of extracellular iodide, by addition of 50 µl standard buffer containing activating compounds

6

167 (forskolin or forskolin + VX-770 both to reach final concentrations of 10 μM). After a further

168 230 s, by which time CFTR is assumed to be gating at steady state (Langron et al., 2018), 100

169 mM extracellular iodide (final concentration) was introduced by adding 50 µl of iodide buffer

170 (as standard buffer with 140 mM NaCl replaced with 400 mM NaI). Images were taken for 40

171 more seconds. Activating compounds were also included in the second addition so as not to

172 alter final extracellular concentrations.

173

174 *Image analysis*

175   Image analysis was automated using MATLAB mathematical computing software

176 (MathWorks). Separate analysis protocols were implemented to estimate CFTR membrane

177 density and ion channel function.

178

179 <u>CFTR membrane density</u>

180   First, mCherry images were binarized, and basic morphological operations (opening,

181 closing, area opening, and dilation) were carried out to reduce noise. A distance transform with

182 locally imposed minima was used to segment images by means of a watershed transformation

183 and define cell boundaries. Cells were removed from analysis if they had an area of under 108

184 μm^2 or over 5400 μm^2, if they had a major axis length of less than 32.4 µm, if the area over

185 perimeter was less than 25 or over 300, and if they were touching the edge of the image. A 1.08

186 µm band, 10 or 5 pixels wide (depending on the resolution of the image), within the border of

187 each cell was defined as the membrane zone.

188   Background was selected by inverting the binarized and morphologically opened

189 mCherry image, after which it was morphologically closed using a large structuring element to

190 prevent cells from being selected as background. Average background intensity was then

191 subtracted from each pixel, and the YFP and mCherry fluorescence intensity of each cell was

192 normalized to the median YFP and mCherry fluorescence intensities of cells expressing WT-

193 CFTR on the same plate. If the average normalized fluorescence intensity fell below 0 (due to

194 low transfection efficiency and high background noise), cells were removed from analysis.

195   In order to estimate CFTR membrane density for each cell (defined as ρ, see Results),

196 the average normalized YFP fluorescence intensity within the membrane zone was divided by

197 the average normalized mCherry fluorescence over the entire cell.

198
$$\rho = \frac{F_{\text{YFP membrane}}}{F_{\text{mCherry cell}}}$$

199

7

200   <u>CFTR ion channel function</u>

201   For assessment of CFTR function, two different protocols were used. For both, cells

202   were selected based on the mCherry fluorescence image that was taken at the beginning of the

203   protocol.

204   (A) I⁻ first Protocol

205   The fluorescence at the time point before addition of I⁻ was used to normalize YFP

206   fluorescence intensity. The concentration of I⁻ inside the cells ($[I^-]_{in}$) can be estimated with the

207   following equation (Langron et al., 2017), in which the binding affinity for I⁻ (K_I) to

208   YFP(H148Q/I152L) is 1.9 mM (Galietta et al., 2001a) and the normalized fluorescence

209   intensity over time ($F(t)$) is determined experimentally.

210
$$[I^-]_{in} = K_I \frac{(1 - F(t))}{F(t)}$$

211   Data is collected every 2 seconds, so the change $[I^-]_{in}$ observed at each time point can be

212   estimated and used to calculate the rate of I⁻ entry (in mM/s):

213
$$\frac{\Delta[I^-]_{in}}{\Delta t} = \frac{[I^-]_{in}(t) - [I^-]_{in}(t-1)}{2 \text{ s}}$$

214   The maximal observed rate of I⁻ entry is used as a measure of cellular anion conductance. To

215   determine whether there was increased CFTR-mediated anion conductance, the maximal rate

216   of I⁻ entry after addition of forskolin (which activates CFTR by cAMP dependent

217   phosphorylation), was compared to the maximal rate of I⁻ entry after addition of DMSO

218   (vehicle, negative control).

219   (B) I⁻ last Protocol

220   CFTR activation (by addition of 10 μM forskolin with or without 10 μM VX-770, as

221   indicated) was first allowed to reach steady state in the absence of I⁻ and quenching of YFP in

222   the 40 s following extracellular I⁻ addition was measured. A simple mathematical model was

223   used to fit observed fluorescence quenching, and estimate CFTR conductance as described

224   (Langron et al., 2018). Briefly, the model includes four free parameters: CFTR conductance at

225   steady-state (G_{CFTR}), membrane potential at steady-state, immediately prior to I⁻ addition (V_M),

226   and conductance (G_{trans}) and time constant (τ_{trans}) of a transient, endogenous non-CFTR anion

227   conductance. The values of the four parameters were estimated by minimizing the sum of

228   squared residuals obtained by comparing the time course of the observed average fluorescence

229   intensity within cells to the proportion of anion-free YFP chromophore predicted by the model

230   (both normalized to the time point before I⁻ addition). However, when the quenching time

231   course was too fast and did not provide enough information to uniquely identify all four

232 parameters, the value of the latter two parameters (G_{trans} and τ_{trans}) was constrained to the

233 average values obtained with negative controls, and only G_{CFTR} and V_M were estimated

234 (Langron et al., 2018).

235   For both protocol (A) and (B) the value obtained from analysis of the observed YFP-

236 CFTR fluorescence quenching ($\frac{\Delta[I^-]_{in}}{\Delta t}$ and G_{CFTR}, respectively) was corrected to account for

237 variations in transfection efficiency. Thus the metric reporting ion channel function was

238 normalised for each condition/genotype by dividing by the mean $F_{mCherry}$ within the cell

239 selection (which, in turn, was normalized to $F_{mCherry}$ measured for WT in the same plate).

240

Data and Statistical analysis

242   Measurements of conductance from the rare mutation panel were obtained on 3 or 4

243 independent plates (each plate containing at least 3 wells per mutant, per condition). As

244 demonstrated by the good correlation with published datasets (see Results and Supplementary

245 Figure S8) this is sufficient to give a first characterization of ion channel function, as is required

246 for most screens. Because ρ values approach a log-normal distribution, values were log

247 transformed before performing statistical analysis, allowing parametric testing of the data.

248   To determine whether the observed differences in ρ, $\frac{\Delta[I^-]_{in}}{\Delta t}$, or G_{CFTR} resulting from

249 experimental manipulation and/or mutations were statistically significant, we performed either

250 independent or paired t-tests. For ρ measurements, we noticed that some variability could be

251 accounted for by variation among plates, and paired comparisons between

252 treatments/genotypes measured from the same plate increased our power to detect small

253 differences. When required, either a Bonferroni or a Benjamini-Hochberg correction was

254 applied to adjust for multiple comparisons. Data in graphs represent mean $\pm$ SEM, and the

255 significance level was pre-specified as $\alpha = 0.05$. Statistical analysis was carried out using

256 MATLAB (MathWorks), SigmaPlot (Systat Software), SPSS (IBM), or Excel (Microsoft).

257

Supplemental Material

259 Tables are given with more information on the statistical analyses performed (S1-S4, S6, S7).

260 Figure S5 compares distributions of $\log_{10}\rho$ values of WT-CFTR with each mutant in the rare

261 mutation panel, as well as plots illustrating the paired t-tests performed. Figure S8 compares

262 the rare mutation results presented here with two published datasets (Sosnay et al., 2013; Van

263 Goor et al., 2014). Figure S9 and Table S10 give further information regarding the analysis

264 used to obtain Figures 4B and 5A.

265

266 **Results**

267 *The assay*

268   To obtain quantitative information about ion channel function of CFTR, we exploited

269 a halide-sensitive YFP (Galietta et al., 2001a; Galietta et al., 2001b), tagged to the N-terminal

270 of CFTR (Langron et al., 2018; Langron et al., 2017). We constructed a pIRES2-mCherry-

271 YFPCFTR plasmid that directs co-expression of YFP(H148Q/I152L)-CFTR (hereafter

272 designated YFP-WT-CFTR or simply WT-CFTR) and a soluble, cytosolic, red fluorescent

273 protein, mCherry (Shaner et al., 2004) (Figure 1A). The mCherry expression allows image

274 segmentation and localization of the cell membrane by marking the border of cells.

275 Furthermore, mCherry serves as an internal standard for the normalisation of YFP-CFTR

276 expression, eliminating variability due to unequal transfection efficiency.

277   Yellow fluorescence at the boundaries of areas of red fluorescence is used to estimate

278 CFTR membrane density for each cell (Figure 1). The "membrane" is defined as comprising a

279 ~1 μm wide band, on the inside of a cell's boundary. The density of CFTR at the membrane

280 (ρ), is estimated by dividing the average YFP-CFTR fluorescence intensity within the

281 membrane zone ($F_{\text{YFP membrane}}$), by the average mCherry fluorescence over the entire cell

282 ($F_{\text{mCherry cell}}$). The ρ metric can be thought of as the product of the proportion of CFTR localized

283 to the membrane ($F_{\text{YFP membrane}}/F_{\text{YFP cell}}$), multiplied by the metabolic stability of YFP-CFTR

284 with respect to mCherry ($F_{\text{YFP cell}}/F_{\text{mCherry cell}}$). Thus, changes in ρ metric will reflect not only

285 changes in CFTR trafficking, but also changes in the overall rates of biosynthesis vs.

286 degradation of the protein.

287

288 *Increasing F508del-CFTR membrane density*

289   To validate our assay, we assessed changes in F508del-CFTR membrane density by

290 comparing distributions of $\log_{10}\rho$ (logarithmic transformation of the ρ metric) obtained from

291 thousands of cells for each genotype/condition (Figure 2).

292

293 F508del-CFTR: VX-809 incubation

294 At 37°C, incubation with VX-809 for 24 hours caused a small but significant increase in $\log_{10}\rho$

295 of F508del-CFTR, (Figure 2A left, see also Supplementary Table S1). At 28°C, the magnitude

296 of the increase was greater (Figure 2A right).

297

298 F508del-CFTR: R1070W second-site revertant mutation

10

299 Introducing the second-site revertant mutation R1070W (Thibodeau et al., 2010) in the

300 F508del-CFTR background, significantly increased membrane density at 37°C, (Figure 2B left,

301 Supplementary Table S1), as well as at 28°C (Figure 2B right, Supplementary Table S1).

302 Again, the magnitude of the effect was larger at 28°C.

303

304 F508del-CFTR: chronic VX-770 incubation

305 When comparing cells expressing F508del-CFTR incubated for 24 hours with VX-809 alone,

306 with those incubated with both VX-809 and VX-770, at 37°C, there was a small but significant

307 decrease in $\log_{10}\rho$ (Figure 2C left, Supplementary Table S1). At 28°C the decrease was again

308 more pronounced than at 37°C (Figure 2C right).

309

310 F508del-CFTR: temperature correction

311 Because our fluorescence readings are normalized to those obtained from cells expressing WT-

312 CFTR grown on the same 96-well plate, we quantified the difference between the mean $\log_{10}\rho$

313 of WT-CFTR and F508del-CFTR at each temperature. The $\log_{10}\rho$ values of F508del-CFTR

314 were found to be significantly closer to those of WT-CFTR at 28°C, than at 37°C, (Figure 2D,

315 Supplementary Table S1).

316

317 *Increasing F508del-CFTR ion channel function*

318 Following addition of extracellular I$^-$ (I$^-$ first Protocol, see Methods), CFTR was

319 activated by 10 µM forskolin alone, or by a combination of 10 µM forskolin and 10 µM VX-

320 770 (the latter defined as an acute (a) treatment, as opposed to the 24-hour chronic (c)

321 incubation with VX-770 described above). The normalized fluorescence of HEK293-cells

322 expressing YFP-tagged WT-CFTR, F508del-CFTR, or F508del/R1070W-CFTRwas followed

323 over time (Figure 3). The maximal rate of I$^-$ entry was used to summarize CFTR channel

324 function for the different CFTR genotypes, incubation and activation conditions tested (Figure

325 3E, Supplementary Tables S2 and S3). No significant difference in this metric was detected

326 among the different genotypes/conditions when DMSO (vehicle) was added instead of

327 activators.

328

329 WT-CFTR

330 As expected, in cells expressing WT-CFTR, the maximal rate of I$^-$ entry was significantly

331 higher after activation with forskolin, compared to control (DMSO), at both 37°C and 28°C

332 (Figure 3A; Figure 3E WT). However, neither the presence of 10 µM VX-770 in addition to

333 forskolin during activation, nor incubation at 37°C vs. 28°C modified quenching rate

334 sufficiently to achieve statistical significance after multiple comparison correction (Figure 3A;

335 Figure 3E, WT, Supplementary Table S3).

336

337 <u>F508del-CFTR: activation following temperature correction</u>

338 Activation with forskolin alone failed to increase the maximal rate of I^- entry in untreated cells

339 expressing F508del-CFTR (Figure 3B top; Figure 3E F508del bars 1 and 4, Supplementary

340 Table S2), reflecting the severe gating defect which persists even after temperature correction.

341 Acute potentiation by VX-770 was required to detect function of the channels reaching the cell

342 surface thanks to temperature-correction (Figure 3B, bottom; Figure 3E F508del bars 5 vs. 2,

343 Supplementary Table S2).

344

345 <u>F508del-CFTR: activation following VX-809 correction</u>

346 At both temperatures, the activity of F508del-CFTR channels reaching the cell surface after

347 24-hour incubation with VX-809 could be detected following acute activation with forskolin

348 and VX-770. At 28°C the maximal rate of I^- entry was significantly greater than at 37°C (Figure

349 3C; Figure 3E, F508del bar 6 vs. 3, Supplementary Table S3).

350

351 <u>F508del-CFTR: rescue of ion channel function by the R1070W mutation</u>

352 Forskolin activation alone was enough to reveal F508del/R1070W-CFTR channel activity

353 (Figure 3D, Supplementary Table S2). The maximal rate of I^- entry was significantly higher at

354 28°C than at 37°C (Figure 3D; Figure 3E F508del/R1070W, Supplementary Table S3).

355

356 *The rare mutation panel*

357 CF-causing missense CFTR mutations (Sosnay et al., 2013; Van Goor et al., 2014; Yu

358 et al., 2012) were individually introduced in the pIRES2-mCherry-YFPCFTR plasmid, creating

359 a panel of 62 plasmids (including WT-CFTR as reference).

360 Following expression of the panel in HEK293 cells, and incubation with no

361 pharmacological correction, distributions for the ρ metric, and plate $\log_{10}\rho$ means were

362 obtained (Supplementary Table S4, Supplementary Figure S5). The data is summarized in

363 Figure 4A, which profiles membrane density for each CFTR mutant in the panel. Correlation

364 between our measured ρ and the proportion of CFTR acquiring complex glycosylation in FRT

365   cells is surprisingly good ($r^2 = 0.65$, Sosnay et al., 2013; $r^2 = 0.48$, Van Goor et al., 2014,

366   Supplementary Figure S8), considering the differences in expression system and metric used

367   (note that correlation between the two published datasets is $r^2 = 0.48$).

368   YFP-CFTR fluorescence quenching experiments (I^- last Protocol, see Methods) were

369   carried out to estimate steady-state CFTR conductance (G_{CFTR}), without (DMSO) and with

370   baseline CFTR activation by 10 µM forskolin (Figure 4B-C; Supplementary Table S6). Again,

371   results correlate well with published data ($r^2 = 0.68$, Sosnay et al., 2013; $r^2 = 0.60$ Van Goor et

372   al., 2014; Supplementary Figure S8). Conductance was also measured in the presence of 10

373   µM forskolin + 10 µM VX-770 (Figure 4B, D; Supplementary Table S7). In these conditions,

374   genotypes with high conductance (including WT-CFTR) have faster YFP quenching than can

375   be reliably measured in our system. However, the assay can accurately monitor VX-770

376   potentiation when CFTR activity is low, as is the case for most mutants (Van Goor et al., 2014).

377

Relationship between CFTR ion channel function and membrane density

379   By considering the changes in ion channel function in the context of any changes

380   measured in ρ, our assay allows more accurate inferences on the gating and permeation

381   properties of the CFTR channel molecules present at the cell surface.

382   Even when virtually no channels are present in the plasma membrane (as happens, for

383   instance, for cells expressing F508del-CFTR incubated at 37^0 C) the value of ρ does not fall to

384   zero. This is likely due to some inaccuracy in automated cell boundary detection and to the

385   widefield microscope optics, resulting in stray light from out-of-focus planes reaching the

386   photomultiplier. To empirically investigate the relationship between G_{CFTR} and ρ, cells

387   expressing F508del-CFTR were treated with increasing concentrations of corrector VX-809,

388   progressively improving both biogenesis/membrane stability and conductance (Figure 5A;

389   Supplementary Figure S9). Measured G_{CFTR} values as a function of ρ values show a roughly

390   linear relationship. The trendline can be extended to cross the ρ axis, extrapolating to an

391   intercept at $\rho = 0.23$. In addition, extension towards higher membrane densities shows how

392   gating of F508del-CFTR, VX-809-corrected and acutely potentiated by VX-770, reaches levels

393   characteristic of WT-CFTR (without potentiation), consistent with patch-clamp open

394   probability (P_O) measurements (Kopeikin et al., 2014; Wang et al., 2018).

395   Data on maximum rate of I⁻ entry can also be plotted against the corresponding ρ values,

396   measured for the different F508del-CFTR rescue strategies (Figure 5B). A linear interpolation

397   between data points for uncorrected F508del-CFTR at 37^0 C (representing cells with virtually

398   no CFTR molecules at the membrane) and WT-CFTR activated by 10 μM forskolin at 37^0 C

399   describes the ion channel function we would expect from cells with increasing CFTR

400   membrane density, assuming gating and permeation characteristics of baseline-activated WT-

401   CFTR. This allows us to infer how rescued F508del-CFTR channels reaching the membrane

402   compare to control channels in terms of function.

403   Introducing the R1070W revertant mutation in the F508del-CFTR background is shown

404   to be particularly effective in improving gating. Comparing revertant rescue with temperature

405   correction, Figure 5B shows how both strategies similarly increase membrane density but

406   temperature-corrected F508del-CFTR channels at the membrane have very low ion channel

407   function (unless acutely potentiated with VX-770). In contrast, F508del/R1070W channels at

408   the membrane have gating and permeation properties equal - or even superior - to WT-CFTR

409   (Figure 5B, cf. F508del/R1070W-CFTR red symbol vs. uncorrected F508del-CFTR blue

410   symbol). Both results are consistent with patch-clamp records indicating a F508del/R1070W-

411   CFTR P_O comparable to that of WT-CFTR (Liu et al., 2018), but a much lower P_O for

412   temperature-corrected F508del-CFTR (Kopeikin et al., 2014; Liu et al., 2018; Wang et al.,

413   2018) – note that single-channel conductance, γ, is unaffected by F508del and R1070W

414   mutations (Dalemans et al., 1991; Thibodeau et al., 2010).

415   Plots of G_{CFTR} as a function of ρ for the rare-mutation panel give an overview of

416   processing and gating/permeation defects caused by each missense mutation (Figure 5C). For

417   instance, D579G-CFTR (orange open diamond at coordinates (0.35,41.5)) falls close to the

418   WT-CFTR interpolation line, suggesting that the product of channel P_O and γ is not greatly

419   affected by this mutation, and that the low short-circuit currents measured in FRT cells (Sosnay

420   et al., 2013; Van Goor et al., 2014) are largely caused by the reduced membrane density. For

421   G1244E (orange (0.75,7.2)) and S549N (blue (0.83,11)), likely altering the structure of P- and

422   signature sequence loops, respectively, in site 2, measured ion channel function is much lower

423   than would be expected given the high membrane density. Here low short-circuit currents

424   (Sosnay et al., 2013) are likely due to gating defects. Most mutations give reduced membrane

425   densities and a conductance that falls below the interpolation line, suggesting processing

426   defects as well as some degree of impairment in gating/permeation for the molecules that do

14

427   reach the membrane. We further illustrate the effect of acute treatment with VX-770 for

428   mutations resulting in the strongest potentiation (fold-potentiation >20, Figure 5D). For many

429   of these, data points for potentiated conductance fall above the interpolation line, suggesting

430   that $P_O \cdot \gamma$ is higher than measured for WT-CFTR in baseline-activated conditions.

431

Discussion

Validation of the assay and implications for pharmacological research

434   Many CFTR variants associated with CF, including the most common, F508del-CFTR,

435   are characterized by both processing and functional defects. Rescue of either ion channel

436   function or membrane density alone, is not enough for effective treatment of patients carrying

437   F508del-CFTR (Clancy et al., 2012; Flume et al., 2012), or many other mutations. Therapies

438   combining multiple correctors/potentiators are now seen as most promising (Holguin, 2018).

439   However, potentiators can negatively interfere with corrector action (Cholon et al., 2014; Meng

440   et al., 2017; Veit et al., 2014). Furthermore, it has been suggested that maintaining a clear

441   separation between correctors and potentiators does not usefully describe CFTR pharmacology

442   (Rowe and Verkman, 2013). Practical implementation of distinct potentiator and corrector

443   screens might have biased the search towards combination therapies, hampering discovery of

444   modulators with true dual activity. All this highlights the potential impact of our assay, capable

445   of simultaneously measuring pharmacological effects on membrane localization and on

446   gating/permeation characteristics.

Membrane density

448   Our assay accurately detects changes in membrane density of CFTR, even when such

449   changes are small and the heterogeneity among cells is large. It can pick up the minute

450   difference in membrane density between untreated and VX-809 treated HEK293 cells

451   incubated at 37°C (Figure 2A left). The VX-809 effect is undetectable, unless combined with

452   temperature rescue or revertant mutations, in other systems (e.g. Okiyoneda et al., 2013). The

453   effect of the R1070W mutation on F508del-CFTR membrane density at 37°C is similarly small

454   (Okiyoneda et al., 2013) but our assay detects a significant difference (Figure 2B left). We

455   were also able to confirm that the membrane density of F508del-CFTR is increased at low

456   temperature (Denning et al., 1992; Rennolds et al., 2008; Wang et al., 2008, Figure 2D). The

457   effects of VX-809 treatment (He et al., 2013) and R1070W rescue on membrane density are

458   larger when combined with incubation at low temperature (Figure 2 right). In agreement with

15

459 other studies (Cholon et al., 2014; Meng et al., 2017; Veit et al., 2014), we observed a small

460 but significant shift in $\log_{10}\rho$ following chronic incubation with VX-770, consistent with the

461 potentiator destabilizing F508del-CFTR at the membrane (Figure 2C left). Furthermore, we

462 find that the negative effect of VX-770 on biogenesis appears more pronounced when cells are

463 incubated at 28°C (Figure 2C). It is possible that binding of VX-770 prevents interaction with

464 chaperone(s) which help F508del-CFTR fold and exit the ER in HEK293 cells grown at low

465 temperature (Wang et al., 2008). However, further studies are required to confirm our

466 observation and its physiological relevance. First, at 37°C the small signal from membrane-

467 localised F508del-CFTR might prevent us from accurately quantifying the effect of adding

468 VX-770 to the incubation. Second, given the high [VX-770] used (Csanády and Töröcsik,

469 2019; Matthes et al., 2016), some of the F508del-CFTR destabilization we observe might be

470 linked to formation of precipitates within cellular membranes, which might be more

471 pronounced at the lower temperature. We note, however, that in our HEK293 incubation

472 medium, as in plasma, a large proportion of the drug will be bound to proteins present in the

473 added serum (Matthes et al., 2016).

474 Ion channel function

475   In addition to membrane density, our assay quantifies channel function. Here, the assay

476 is not optimized to measure high CFTR activities and some measurements hit the upper limit

477 of its dynamic range (e.g. for WT-CFTR, Figs. 3 and 4, Supplementary Table S3). However,

478 both the "I⁻ first" protocol (Langron et al., 2017), measuring the maximal rate of I⁻ entry

479 ($\frac{\Delta[I^-]_{in}}{\Delta t}$) during CFTR activation, and "I⁻ last" protocol (Langron et al., 2018), estimating CFTR

480 conductance by fitting quenching time course after steady-state activation is reached, can

481 accurately quantify the low CFTR activities typically seen in mutants. While the "I⁻ last"

482 protocol is unaffected by variability in signal transduction kinetics and better accounts for

483 changing electrochemical potential gradients, the "I⁻ first" protocol allows faster data

484 acquisition and less computationally intensive analysis. In line with results obtained with other

485 techniques (e.g. Ussing chambers, high-throughput electrophysiology), our results show that

486 both G_{CFTR} (Sosnay et al., 2013; Van Goor et al., 2014, Supplementary Figure S8) and $\frac{\Delta[I^-]_{in}}{\Delta t}$

487 (Billet et al., 2017; Van Goor et al., 2011, Figures 3, 5B) provide accurate estimates of CFTR

488 activity.

489   Accurate quantification of low conductance values is advantageous in characterizing

490 drug response by CFTR mutants, most of which have low residual activity. Our assay detects

491 strong VX-770 potentiation for R347P-, N1303K- and H1085R-CFTR, genotypes giving no

16

492 significant potentiation over baseline in the Ussing chamber study (Van Goor et al., 2014).
493 Equally, L927P- and H1045D-CFTR channels are seen to be powerfully potentiated in our
494 assay. Acute treatment with VX-770 is most effective on L927P channels, resulting in an ~80-
495 fold potentiation. L927P is adjacent to A928, part of the VX-770 binding site (Liu et al., 2019).
496 Our results on N1303K are consistent with patch-clamp results demonstrating effective
497 potentiation by VX-770 (DeStefano et al., 2018). Despite Cl$^-$ permeability in FRT cells being
498 increased only to less than 5% of WT-CFTR-expressing cells (Van Goor et al., 2014), caution
499 is required in classifying all such mutants as "unresponsive" to VX-770. Further investigation
500 of possible synergies/drug-drug interactions will be required as it is likely that they might
501 benefit from therapies combining VX-770 with other modulators, as has been proposed
502 (DeStefano et al., 2018; Phuan et al., 2018): patch-clamp recording of how the ion channel
503 function of these mutants is altered by simultaneous binding of VX-770 and other modulators,
504 and studies on chronic rather than acute treatment.

505   While other functional assays, in more native systems (e.g. Ussing chamber
506 measurements on human bronchial epithelia), will remain the "gold standard" for testing of
507 CFTR-targeting drugs, providing licensing authorities with material on which to base decisions
508 on treatment of patients with genotypes found only extremely rarely in the population (Ratner,
509 2017), our assay could usefully complement these and other techniques, especially if
510 throughput is further increased (the assay is currently run using 96-well plates but small
511 changes could make it compatible to a 384 well plate format). Describing each CF-causing
512 mutation with two coordinates (ρ and G$_{CFTR}$) is a concise, informative way of characterizing
513 mutations (e.g. Figure 5C) and the effects of CFTR modulators on them (e.g. Figure 5D).
514 Implementing the assay at early stages (compound screening and structure-activity relationship
515 studies) could better inform development of genotype-tailored therapies and give valuable
516 insight relevant to patient stratification for clinical trial planning. In addition, our high-content
517 assay boosts the potential for discovery of drugs simultaneously repairing both defects
518 (correcting CFTR biogenesis and potentiating its function), and its exploitation might result in
519 successful identification of effective and potent dual-activity modulators, a feat that has so far
520 eluded extensive compound screens (but note proof-of-principle demonstration in Phuan et al.,
521 2015; Phuan et al., 2011).

522

523 *Considerations on VX-770 binding and mechanism of action*

524   Empirical profiling of drug effects on the rare mutation panel can generate hypotheses

525   on mechanism of action. Considering the sites of mutations resulting in the highest VX-770

526   efficacy (fold-potentiation >20, Figure 5D), these appear to link the ATP molecule bound at

527   site 1 (comprising Walker motifs of NBD1 and signature sequence of NBD2) to regions close

528   to the narrowest portion of the permeation pathway, thought to constitute the CFTR gate (El

529   Hiani and Linsdell, 2010; Gao and Hwang, 2015), and positioned adjacent to the very recently

530   identified VX-770 binding site (Liu et al., 2019) (Figure 6).

531   Among the highly VX-770-sensitive mutations, all those surrounding the ATP and

532   NBD/TMD interface introduce charged side chains which would interact unfavourably with

533   other close charges in the conformation observed for phosphorylated, ATP-bound human

534   CFTR, carrying the open-state stabilizing E1371Q mutation, 6MSM (Zhang et al., 2018b): the

535   aspartate replacing G1349, in the NBD2 signature sequence, with the γ-phosphate bound at site

536   1 (Bompadre et al., 2007); the lysine in place of N1303 in the NBD2 "socket", with R1358 in

537   NBD2; the arginine replacing G178, in intracellular loop 1 (ICL1) with K254, E257 and R258

538   in ICL2 (Zhang et al., 2018b); the aspartate replacing H1054, in ICL4, with E543 in the NBD1

539   X-loop (He et al., 2008); the arginine in place of H1085, with R1048 in transmembrane helix

540   10, TM10 (for all listed pairs distances between α-carbons in 6MSM are below 10 Å).

541   Mutations at these sites are likely to particularly destabilize the NBD-dimerized, ABC-

542   canonical open channel conformation, making occupancy of these states a rare event.

543   Consistent with this interpretation, N1303K-CFTR channels appear to have almost completely

544   lost the coupling between NBDs and TMDs that normally controls gating, and the rare openings

545   observed are not linked to ATPase cycles at the NBDs (DeStefano et al., 2018). The fact that

546   for all these mutants conductance is greatly increased by VX-770 suggests that drug binding

547   might allow these channels to reach an alternative, particularly stable, open state, with a

548   different conformation at the interface between site 1 and the TMDs.

549   It has been recently suggested that "undocking" of NBD1 from the TMDs might occur

550   physiologically (Sigoillot et al., 2019) and a recent finding hints at the possibility that the VX-

551   770-bound open state might comprise an undocked NBD1. The coupling helix in ICL4, buried

552   at the interface between TMDs and NBD1 in all the CFTR structures so far reported, was

553   identified as the region for which VX-770 binding decreases hydrogen/deuterium exchange

554   most (Byrnes et al., 2018), as would be expected if this helix forms part of a drug-binding site.

555   While the recent cryo-EM structure of the E1371Q CFTR mutant in complex with VX-770

556   shows density for only one VX-770 molecule, bound in the transmembrane region (Liu et al.,

18

557 2019), it is possible that the exceptionally stable NBD1/NBD2 dimer of this mutant prevents

558 VX-770 access to a second binding site at the ICL4/NBD1 interface. In contrast, in WT and

559 other mutants, NBD1 undocking might expose this second site. It is interesting to note that

560 binding of a drug at a site between TM4, TM5 and TM6 (not far from the transmembrane VX-

561 770 binding site on CFTR) in the MsbA bacterial ABC exporter, leads to a conformational

562 change in TM4 which is transmitted to the NBDs and results in the unusual displacement of

563 one NBD, undocking it from the conserved network of molecular interactions generally

564 observed at the NBD/TMD interface (Ho et al., 2018). NBD undocking in VX-770-bound

565 CFTR, by altering the NBD1/NBD2 interface might result in deocclusion of one of the

566 interfacial ATP-binding sites. Occupancy of this low affinity ATP-binding site, accessible on

567 open channels, might underlie the observed prolongation of open dwell-time with increasing

568 [ATP] (Jih and Hwang, 2013). A second VX-770 binding site, exposed by infrequent

569 undocking of NBD1 would also be consistent with the very slow activation time-course

570 observed upon addition of VX-770 to WT-CFTR, likely reflecting VX-770 having to

571 sequentially occupy two sites before the P_O can increase (Csanády and Töröcsik, 2019).

572 The remaining two highly VX-770-sensitive mutations we identify, R347P and L927P

573 (Figures 5D,6) insert prolines, known to restrict backbone flexibility, in a region close to the

574 CFTR gate. R347, in TM6, is important for maintaining a stable conducting pathway (Cotten

575 and Welsh, 1999; Cui et al., 2013; Kopeikin et al., 2010), while L927 is in the unwound

576 segment of TM8 (Corradi et al., 2018; Liu et al., 2017), underlying CFTR's unique channel

577 function (Liu et al., 2017). The very low conductance measured after baseline activation in

578 both these mutants, suggests that backbone flexibility at both these sites is required for channel

579 opening and/or to maintain an open permeation pathway (Zhang et al., 2018b). VX-770 has

580 been hypothesized to increase conformational flexibility of CFTR (Cholon et al., 2014) overall.

581 It is possible that this increased flexibility might particularly concern regions surrounding

582 bound VX-770 facilitating rearrangement of the helices, allowing adoption of the alternative

583 open state described above.

Conclusions

585 The main advantage of our assay consists in providing simultaneous measurements of

586 ion channel function and membrane density. Currently available high throughput assays report

587 on either CFTR surface expression or CFTR-mediated cellular conductance (G_{CFTR}). G_{CFTR} is

588 the product of 3 factors: the number of channels at the membrane (N), P_O, and γ (i.e. $G_{CFTR} =$

589 $N \cdot P_O \cdot \gamma$). Being able to monitor how compounds or mutations affect both number of channels

19

590   at the membrane and conductance can allow accurate deconvolution of effects on processing

591   (altering N) from those influencing gating and permeation of the channel (affecting P_O and γ,

592   respectively). Thus, used in combination with other techniques (e.g. patch-clamp, molecular

593   dynamics and Ussing chamber measurements), the assay is a powerful tool for basic research

594   on CFTR biophysics and biogenesis, as well as for translational research on CFTR-targeting

595   drugs.

596   Finally, because CFTR plays an important role controlling fluid transport across several

597   epithelia (Frizzell and Hanrahan, 2012; Saint-Criq and Gray, 2017), it has been implicated in

598   a number of pathologies, including COPD (Solomon et al., 2017; Zhao et al., 2014), secretory

599   diarrhoeas (Thiagarajah et al., 2015), polycystic kidney disease (Li et al., 2012) and others

600   (Solymosi et al., 2013; Zhang et al., 2018a). It is likely that, given the complexity of CFTR

601   folding and trafficking (Farinha and Canato, 2017; Lukacs and Verkman, 2012), many CFTR-

602   targeting compounds will alter its cellular processing (Clunes et al., 2012), suggesting that the

603   assay could also be usefully deployed in the development of novel CFTR-targeting drugs for

604   other diseases, beyond CF.

Author Contributions

Experiments were conceived and designed by SP, EL and PV, after discussion with LDG and CH. SP and EL, with the help of ACS, CH and EJH, carried out the molecular biology, ran the fluorescence assay acquisition and ran image analysis. SP, with the help of CH, implemented the image analysis protocols and the mathematical model in the MATLAB environment. Manuscript was written by SP, EL and PV. All authors read and commented on the final draft of the manuscript.

Acknowledgements

Conflict of interest declaration

The authors declare no conflicts of interest.

21

References

Billet A, Froux L, Hanrahan JW, and Becq F (2017). Development of Automated Patch Clamp Technique to Investigate CFTR Chloride Channel Function. Front Pharmacol 8.

Bompadre SG, Sohma Y, Li M, and Hwang T-C (2007). G551D and G1349D, Two CF-associated Mutations in the Signature Sequences of CFTR, Exhibit Distinct Gating Defects. J Gen Physiol 129: 285-298.

Byrnes LJ, Xu Y, Qiu X, Hall JD, and West GM (2018). Sites associated with Kalydeco binding on human Cystic Fibrosis Transmembrane Conductance Regulator revealed by Hydrogen/Deuterium Exchange. Scientific Reports 8: 4664.

Cholon DM, Quinney NL, Fulcher ML, Esther CR, Das J, Dokholyan NV, et al. (2014). Potentiator ivacaftor abrogates pharmacological correction of deltaF508 CFTR in cystic fibrosis. Sci Transl Med 6: 246ra296.

Clancy JP, Rowe SM, Accurso FJ, Aitken ML, Amin RS, Ashlock MA, et al. (2012). Results of a phase IIa study of VX-809, an investigational CFTR corrector compound, in subjects with cystic fibrosis homozygous for the F508del-CFTR mutation. Thorax 67: 12-18.

Clunes LA, Davies CM, Coakley RD, Aleksandrov AA, Henderson AG, Zeman KL, et al. (2012). Cigarette smoke exposure induces CFTR internalization and insolubility, leading to airway surface liquid dehydration. FASEB J 26: 533-545.

Corradi V, Gu R-X, Vergani P, and Tieleman DP (2018). Structure of Transmembrane Helix 8 and Possible Membrane Defects in CFTR. Biophys J 114: 1751-1754.

Cotten JF, and Welsh MJ (1999). Cystic Fibrosis-associated Mutations at Arginine 347 Alter the Pore Architecture of CFTR. Evidence for disruption of a salt bridge. J Biol Chem 274: 5429-5435.

Csanády L, and Töröcsik B (2019). Cystic fibrosis drug ivacaftor stimulates CFTR channels at picomolar concentrations. eLife 8: e46450.

653

654   Csanády L, Vergani P, and Gadsby DC (2019). STRUCTURE, GATING, AND

655   REGULATION OF THE CFTR ANION CHANNEL. Physiol Rev 99: 707-738.

656

657   Cui G, Freeman CS, Knotts T, Prince CZ, Kuang C, and McCarty NA (2013). Two Salt

658   Bridges Differentially Contribute to the Maintenance of Cystic Fibrosis Transmembrane

659   Conductance Regulator (CFTR) Channel Function. J Biol Chem 288: 20758-20767.

660

661   Dalemans W, Barbry P, Champigny G, Jallat S, Jallat S, Dott K, et al. (1991). Altered

662   chloride ion channel kinetics associated with the [Delta]F508 cystic fibrosis mutation. Nature

663   354: 526-528.

664

665   Davies JC, Moskowitz SM, Brown C, Horsley A, Mall MA, McKone EF, et al. (2018). VX-

666   659–Tezacaftor–Ivacaftor in Patients with Cystic Fibrosis and One or Two Phe508del

667   Alleles. N Engl J Med 379: 1599-1611.

668

669   Denning GM, Anderson MP, Amara JF, Marshall J, Smith AE, and Welsh MJ (1992).

670   Processing of mutant cystic fibrosis transmembrane conductance regulator is temperature-

671   sensitive. Nature 358: 761-764.

672

673   DeStefano S, Gees M, and Hwang T-C (2018). Physiological and pharmacological

674   characterization of the N1303K mutant CFTR. Journal of Cystic Fibrosis.

675

676   El Hiani Y, and Linsdell P (2010). Changes in Accessibility of Cytoplasmic Substances to the

677   Pore Associated with Activation of the Cystic Fibrosis Transmembrane Conductance

678   Regulator Chloride Channel. J Biol Chem 285: 32126-32140.

679

680   Elborn JS (2016). Cystic fibrosis. The Lancet 388: 2519-2531.

681

682   Farinha CM, and Canato S (2017). From the endoplasmic reticulum to the plasma membrane:

683   mechanisms of CFTR folding and trafficking. cell Mol Life Sci 74: 39-55.

684

685   Farinha CM, King-Underwood J, Sousa M, Correia Ana R, Henriques Barbara J, Roxo-Rosa

686   M, et al. (2013). Revertants, Low Temperature, and Correctors Reveal the Mechanism of

687   F508del-CFTR Rescue by VX-809 and Suggest Multiple Agents for Full Correction. Chem

688   Biol 20: 943-955.

690   Flume PA, Liou TG, Borowitz DS, Li H, Yen K, Ordoñez CL, et al. (2012). Ivacaftor in

691   subjects with cystic fibrosis who are homozygous for the f508del-cftr mutation. Chest 142:

692   718-724.

694   Frizzell RA, and Hanrahan JW (2012). Physiology of Epithelial Chloride and Fluid Secretion.

695   Cold Spring Harb Perspect Med 2.

697   Galietta L, Haggie P, and Verkman A (2001a). Green fluorescent protein-based halide

698   indicators with improved chloride and iodide affinities. FEBS Lett 499: 220-224.

700   Galietta L, Jayaraman S, and Verkman A (2001b). Cell-based assay for high-throughput

701   quantitative screening of CFTR chloride transport agonists. Am J Physiol Cell Physiol 281:

702   C1734-C1742.

704   Gao X, and Hwang T-C (2015). Localizing a gate in CFTR. Proceedings of the National

705   Academy of Sciences of the United States of America 112: 2461-2466.

707   Gentzsch M, and Mall MA (2018). Ion Channel Modulators in Cystic Fibrosis. Chest 154:

708   383-393.

710   He L, Aleksandrov AA, Serohijos AWR, Hegedus T, Aleksandrov LA, Cui L, et al. (2008).

711   Multiple Membrane-Cytoplasmic Domain Contacts in the Cystic Fibrosis Transmembrane

712   Conductance Regulator (CFTR) Mediate Regulation of Channel Gating. J Biol Chem 283:

713   26383-26390.

715   He L, Kota P, Aleksandrov AA, Cui L, Jensen T, Dokholyan NV, et al. (2013). Correctors of

716   deltaF508 CFTR restore global conformational maturation without thermally stabilizing the

717   mutant protein. FASEB J 27: 536-545.

719   Ho H, Miu A, Alexander MK, Garcia NK, Oh A, Zilberleyb I, et al. (2018). Structural basis

720   for dual-mode inhibition of the ABC transporter MsbA. Nature 557: 196-201.

24

721

722　Holguin F (2018). Triple CFTR Modulator Therapy for Cystic Fibrosis. N Engl J Med 379:

723　1671-1672.

724

725　Jih K-Y, and Hwang T-C (2013). Vx-770 potentiates CFTR function by promoting

726　decoupling between the gating cycle and ATP hydrolysis cycle. Proceedings of the National

727　Academy of Sciences of the United States of America 110: 4404-4409.

728

729　Keating D, Marigowda G, Burr L, Daines C, Mall MA, McKone EF, et al. (2018). VX-445–

730　Tezacaftor–Ivacaftor in Patients with Cystic Fibrosis and One or Two Phe508del Alleles.

731　New England Journal of Medicine 379: 1612-1620.

732

733　Kopeikin Z, Sohma Y, Li M, and Hwang T-C (2010). On the mechanism of CFTR inhibition

734　by a thiazolidinone derivative. J Gen Physiol 136: 659.

735

736　Kopeikin Z, Yuksek Z, Yang HY, and Bompadre SG (2014). Combined effects of VX-770

737　and VX-809 on several functional abnormalities of F508del-CFTR channels. Journal of

738　Cystic Fibrosis 13: 508-514.

739

740　Langron E, Prins S, and Vergani P (2018). Potentiation of the cystic fibrosis transmembrane

741　conductance regulator by VX-770 involves stabilization of the pre-hydrolytic, O1 state. Br J

742　Pharmacol 175: 3990-4002.

743

744　Langron E, Simone MI, Delalande CMS, Reymond J-L, Selwood DL, and Vergani P (2017).

745　Improved fluorescence assays to measure the defects associated with F508del-CFTR allow

746　identification of new active compounds. Br J Pharmacol 174: 525-539.

747

748　Li H, Yang W, Mendes F, Amaral MD, and Sheppard DN (2012). Impact of the cystic

749　fibrosis mutation F508del-CFTR on renal cyst formation and growth. Am J Physiol Renal

750　Physiol 303: F1176-F1186.

751

752　Lin S-C, Karoly ED, and Taatjes DJ (2013). The human ΔNp53 isoform triggers metabolic

753　and gene expression changes that activate mTOR and alter mitochondrial function. Aging

754　Cell 12: 863-872.

25

755

756 Liu F, Zhang Z, Csanády L, Gadsby DC, and Chen J (2017). Molecular Structure of the

757 Human CFTR Ion Channel. Cell 169: 85-95.e88.

758

759 Liu F, Zhang Z, Levit A, Levring J, Touhara KK, Shoichet BK, et al. (2019). Structural

760 identification of a hotspot on CFTR for potentiation. Science 364: 1184-1188.

761

762 Liu J, Bihler H, Farinha CM, Awatade NT, Romão AM, Mercadante D, et al. (2018). Partial

763 rescue of F508del-cystic fibrosis transmembrane conductance regulator channel gating with

764 modest improvement of protein processing, but not stability, by a dual-acting small molecule.

765 Br J Pharmacol 175: 1017-1038.

766

767 Lukacs GL, and Verkman AS (2012). CFTR: folding, misfolding and correcting the

768 [delta]F508 conformational defect. Trends Mol Med 18: 81-91.

769

770 Ma T, Vetrivel L, Yang H, Pedemonte N, Zegarra-Moran O, Galietta LJV, et al. (2002).

771 High-affinity Activators of Cystic Fibrosis Transmembrane Conductance Regulator (CFTR)

772 Chloride Conductance Identified by High-throughput Screening. J Biol Chem 277: 37235-

773 37241.

774

775 Matthes E, Goepp J, Carlile GW, Luo Y, Dejgaard K, Billet A, et al. (2016). Low free drug

776 concentration prevents inhibition of F508del CFTR functional expression by the potentiator

777 VX-770 (ivacaftor). British Journal of Pharmacology 173: 459-470.

778

779 Meng X, Wang Y, Wang X, Wrennall JA, Rimington TL, Li H, et al. (2017). Two Small

780 Molecules Restore Stability to a Subpopulation of the Cystic Fibrosis Transmembrane

781 Conductance Regulator with the Predominant Disease-causing Mutation. J Biol Chem 292:

782 3706-3719.

783

784 Okiyoneda T, Veit G, Dekkers JF, Bagdany M, Soya N, Xu H, et al. (2013). Mechanism-

785 based corrector combination restores deltaF508-CFTR folding and function. Nat Chem Biol

786 9: 444-454.

787

788 Pedemonte N, Lukacs GL, Du K, Caci E, Zegarra-Moran O, Galietta LJV, et al. (2005a).

789 Small-molecule correctors of defective [Delta]F508-CFTR cellular processing identified by

790 high-throughput screening. J Clin Invest 115: 2564-2571.

791

792 Pedemonte N, Sonawane ND, Taddei A, Hu J, Zegarra-Moran O, Suen YF, et al. (2005b).

793 Phenylglycine and Sulfonamide Correctors of Defective [Delta]F508 and G551D Cystic

794 Fibrosis Transmembrane Conductance Regulator Chloride-Channel Gating. Mol Pharmacol

795 67: 1797-1807.

796

797 Phuan P-W, Son J-H, Tan J-A, Li C, Musante I, Zlock L, et al. (2018). Combination

798 potentiator ('co-potentiator') therapy for CF caused by CFTR mutants, including N1303K,

799 that are poorly responsive to single potentiators. Journal of Cystic Fibrosis.

800

801 Phuan P-W, Veit G, Tan J, Finkbeiner WE, Lukacs GL, and Verkman AS (2015).

802 Potentiators of Defective ΔF508-CFTR Channel Gating that do not Interfere with Corrector

803 Action. Mol Pharmacol 88: 791-799.

804

805 Phuan P-W, Yang B, Knapp JM, Wood AB, Lukacs GL, Kurth MJ, et al. (2011).

806 Cyanoquinolines with Independent Corrector and Potentiator Activities Restore

807 [delta]Phe508-Cystic Fibrosis Transmembrane Conductance Regulator Chloride Channel

808 Function in Cystic Fibrosis. Mol Pharmacol 80: 683-693.

809

810 Ratner M (2017). FDA deems in vitro data on mutations sufficient to expand cystic fibrosis

811 drug label. Nature Biotechnology 35: 606.

812

813 Rennolds J, Boyaka PN, Bellis SL, and Cormet-Boyaka E (2008). Low temperature induces

814 the delivery of mature and immature CFTR to the plasma membrane. Biochem Biophys Res

815 Commun 366: 1025-1029.

816

817 Riordan JR, Rommens JM, Kerem B, Alon N, Rozmahel R, Grzelczak Z, et al. (1989).

818 Identification of the cystic fibrosis gene: cloning and characterization of complementary

819 DNA. Science 245: 1066-1073.

820

821   Rommens JM, Iannuzzi MC, Kerem B-s, Drumm ML, Melmer G, Dean M, et al. (1989).

822   Identification of the Cystic Fibrosis Gene: Chromosome Walking and Jumping. Science 245:

823   1059-1065.

824

825   Rowe SM, and Verkman AS (2013). Cystic Fibrosis Transmembrane Regulator Correctors

826   and Potentiators. Cold Spring Harb Perspect Med 3: a009761.

827

828   Saint-Criq V, and Gray MA (2017). Role of CFTR in epithelial physiology. Cellular and

829   Molecular Life Sciences 74: 93-115.

830

831   Shaner NC, Campbell RE, Steinbach PA, Giepmans BNG, Palmer AE, and Tsien RY (2004).

832   Improved monomeric red, orange and yellow fluorescent proteins derived from Discosoma

833   sp. red fluorescent protein. Nat Biotechnol 22: 1567.

834

835   Sigoillot M, Overtus M, Grodecka M, Scholl D, Garcia-Pino A, Laeremans T, et al. (2019).

836   Domain-interface dynamics of CFTR revealed by stabilizing nanobodies. Nature

837   Communications 10: 2636.

838

839   Solomon GM, Fu L, Rowe SM, and Collawn JF (2017). The therapeutic potential of CFTR

840   modulators for COPD and other airway diseases. Current Opinion in Pharmacology 34: 132-

841   139.

842

843   Solymosi EA, Kaestle-Gembardt SM, Vadász I, Wang L, Neye N, Chupin CJA, et al. (2013).

844   Chloride transport-driven alveolar fluid secretion is a major contributor to cardiogenic lung

845   edema. Proceedings of the National Academy of Sciences of the United States of America

846   110: E2308-E2316.

847

848   Sosnay PR, Siklosi KR, Van Goor F, Kaniecki K, Yu H, Sharma N, et al. (2013). Defining

849   the disease liability of variants in the cystic fibrosis transmembrane conductance regulator

850   gene. Nat Genet 45: 1160-1167.

851

852   Thiagarajah JR, Donowitz M, and Verkman AS (2015). Secretory diarrhoea: mechanisms and

853   emerging therapies. Nat Rev Gastroenterol Hepatol 12: 446-457.

854

855   Thibodeau PH, Richardson JM, Wang W, Millen L, Watson J, Mendoza JL, et al. (2010). The

856   Cystic Fibrosis-causing Mutation deltaF508 Affects Multiple Steps in Cystic Fibrosis

857   Transmembrane Conductance Regulator Biogenesis. J Biol Chem 285: 35825-35835.

858

859   Van Goor F, Hadida S, Grootenhuis PDJ, Burton B, Cao D, Neuberger T, et al. (2009).

860   Rescue of CF airway epithelial cell function in vitro by a CFTR potentiator, VX-770.

861   Proceedings of the National Academy of Sciences of the United States of America 106:

862   18825-18830.

863

864   Van Goor F, Hadida S, Grootenhuis PDJ, Burton B, Stack JH, Straley KS, et al. (2011).

865   Correction of the F508del-CFTR protein processing defect in vitro by the investigational drug

866   VX-809. Proceedings of the National Academy of Sciences of the United States of America

867   108: 18843-18848.

868

869   Van Goor F, Straley KS, Cao D, Gonzalez J, Hadida S, Hazlewood A, et al. (2006). Rescue

870   of [Delta]F508-CFTR trafficking and gating in human cystic fibrosis airway primary cultures

871   by small molecules. Am J Physiol Lung Cell Mol Physiol 290: L1117-1130.

872

873   Van Goor F, Yu H, Burton B, and Hoffman BJ (2014). Effect of ivacaftor on CFTR forms

874   with missense mutations associated with defects in protein processing or function. J Cyst

875   Fibros 13: 29-36.

876

877   Veit G, Avramescu RG, Perdomo D, Phuan P-W, Bagdany M, Apaja PM, et al. (2014). Some

878   gating potentiators, including VX-770, diminish F508del-CFTR functional expression. Sci

879   Transl Med 6: 246ra297.

880

881   Wainwright CE, Elborn JS, Ramsey BW, Marigowda G, Huang X, Cipolli M, et al. (2015).

882   Lumacaftor–Ivacaftor in Patients with Cystic Fibrosis Homozygous for Phe508del CFTR. N

883   Engl J Med 373: 220-231.

884

885   Wang X, Koulov AV, Kellner WA, Riordan JR, and Balch WE (2008). Chemical and

886   Biological Folding Contribute to Temperature-Sensitive ΔF508 CFTR Trafficking. Traffic 9:

887   1878-1893.

888

889   Wang Y, Cai Z, Gosling M, and Sheppard DN (2018). Potentiation of the cystic fibrosis

890   transmembrane conductance regulator Cl− channel by ivacaftor is temperature independent.

891   American Journal of Physiology-Lung Cellular and Molecular Physiology 315: L846-L857.

892

893   Yang H, Shelat AA, Guy RK, Gopinath VS, Ma T, Du K, et al. (2003). Nanomolar Affinity

894   Small Molecule Correctors of Defective [Delta]F508-CFTR Chloride Channel Gating. J Biol

895   Chem 278: 35079-35085.

896

897   Yu H, Burton B, Huang C-J, Worley J, Cao D, Johnson Jr JP, et al. (2012). Ivacaftor

898   potentiation of multiple CFTR channels with gating mutations. J Cyst Fibros 11: 237-245.

899

900   Zhang J, Wang Y, Jiang X, and Chan HC (2018a). Cystic fibrosis transmembrane

901   conductance regulator—emerging regulator of cancer. Cellular and Molecular Life Sciences

902   75: 1737-1756.

903

904   Zhang Z, Liu F, and Chen J (2018b). Molecular structure of the ATP-bound, phosphorylated

905   human CFTR. Proceedings of the National Academy of Sciences of the United States of

906   America.

907

908   Zhao R, Liang X, Zhao M, Liu S-L, Huang Y, Idell S, et al. (2014). Correlation of Apical

909   Fluid-Regulating Channel Proteins with Lung Function in Human COPD Lungs. PLOS ONE

910   9: e109725.

911

912

913   **Figures and figure legends**

914

915   **Figure 1**
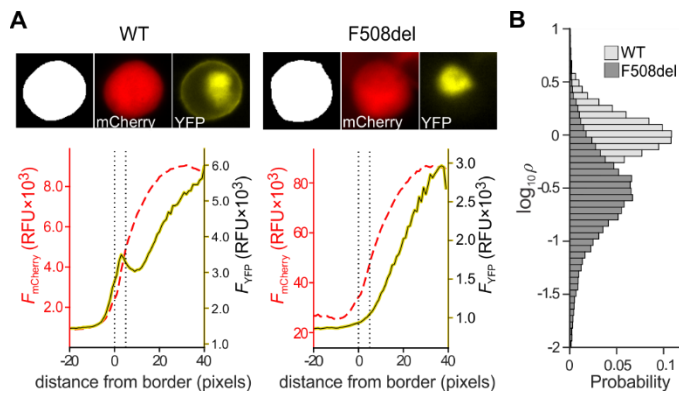
916

917   Image analysis to quantify CFTR membrane density (**A**) Image analysis of individual

918   representative HEK293 cells transfected with pIRES2-mCherry-YFP-WT-CFTR (left), and

919   pIRES2-mCherry-YFP-F508del-CFTR (right). Upper panels: boundary delimiting cell (white)

920   from non-cell (black) is obtained from mCherry image (centre). CFTR cellular localization is

921   obtained from YFP image (right). Lower panels: average mCherry fluorescence intensity

922   ($F_{mCherry}$, red dashed line), and average YFP fluorescence intensity (F_{YFP}, solid yellow line), as

923   a function of the distance from cell border. Membrane density is defined as

924
$$\rho = \frac{F_{YFP\ membrane}}{F_{mCherry\ cell}}$$

925   where $F_{YFP\ membrane}$ is the average fluorescence intensity within the 'membrane' zone, set

926   between 0 and 5 pixels from the cell border. (**B**) Probability density distribution of $\log_{10}\rho$ for

927   cells expressing YFP-WT-CFTR (light grey), and YFP-F508del-CFTR (dark grey), incubated

928   at 37 °C. For the representative cells shown in panel A, WT: $\rho = 1.60$; F508del: $\rho = 0.25$.

31
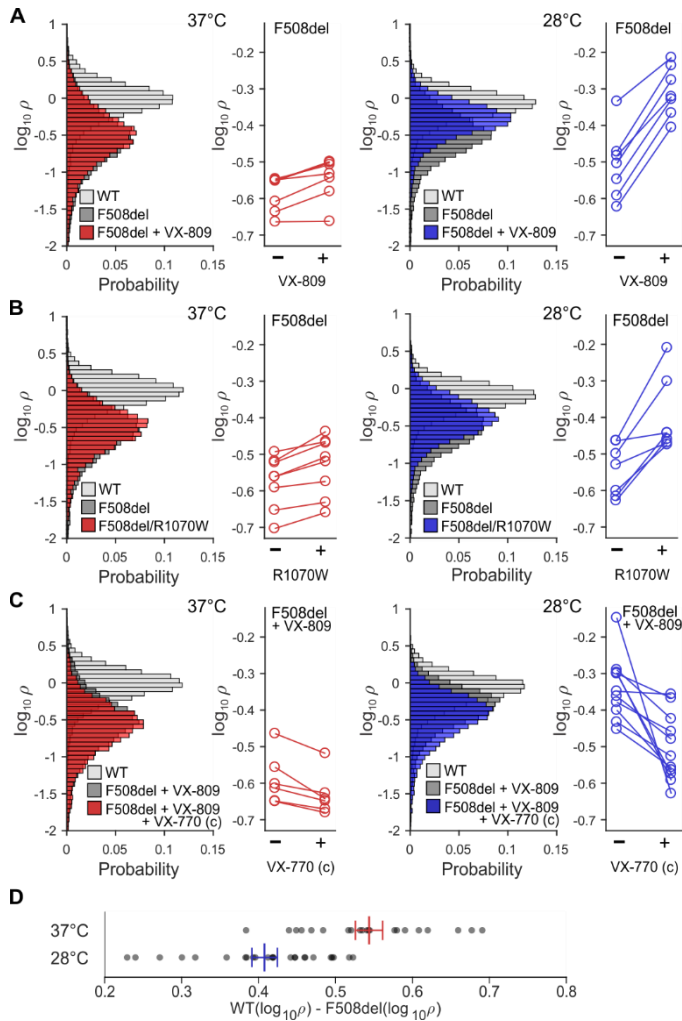
Figure 2

Monitoring CFTR membrane density ($\log_{10}\rho$) in HEK293 cells expressing WT-CFTR, F508del-CFTR, or F508del/R1070W-CFTR. Effects of chronic treatment with 10 µM VX-809 (**A**), R1070W rescue (**B**), and chronic treatment with 10 µM VX-809 + 10 µM VX-770 (**C**), on $\log_{10}\rho$ at 37°C (left, red) and 28°C (right, blue). Conditions of final incubation were maintained during image acquisition. The probability distributions in the panels on the left, contain $\log_{10}\rho$ measurements from thousands of cells, pooled from all experiments. For statistical analysis, mean $\log_{10}\rho$ values determined in independent experiments, and paired per plate, were used (displayed in panels on the right) (**D**) Before imaging, plates were incubated at 37°C, or 28°C for 24 hours. For each plate, the difference between mean $\log_{10}\rho$ for WT-CFTR and F508del-CFTR was calculated (WT($\log_{10}\rho$) - F508del($\log_{10}\rho$), grey dots). Red (37°C) and blue (28°C) lines show mean ± SEM, calculated from 21(37°C) and 25(28°C) within-plate difference estimates.

32

Figure 3
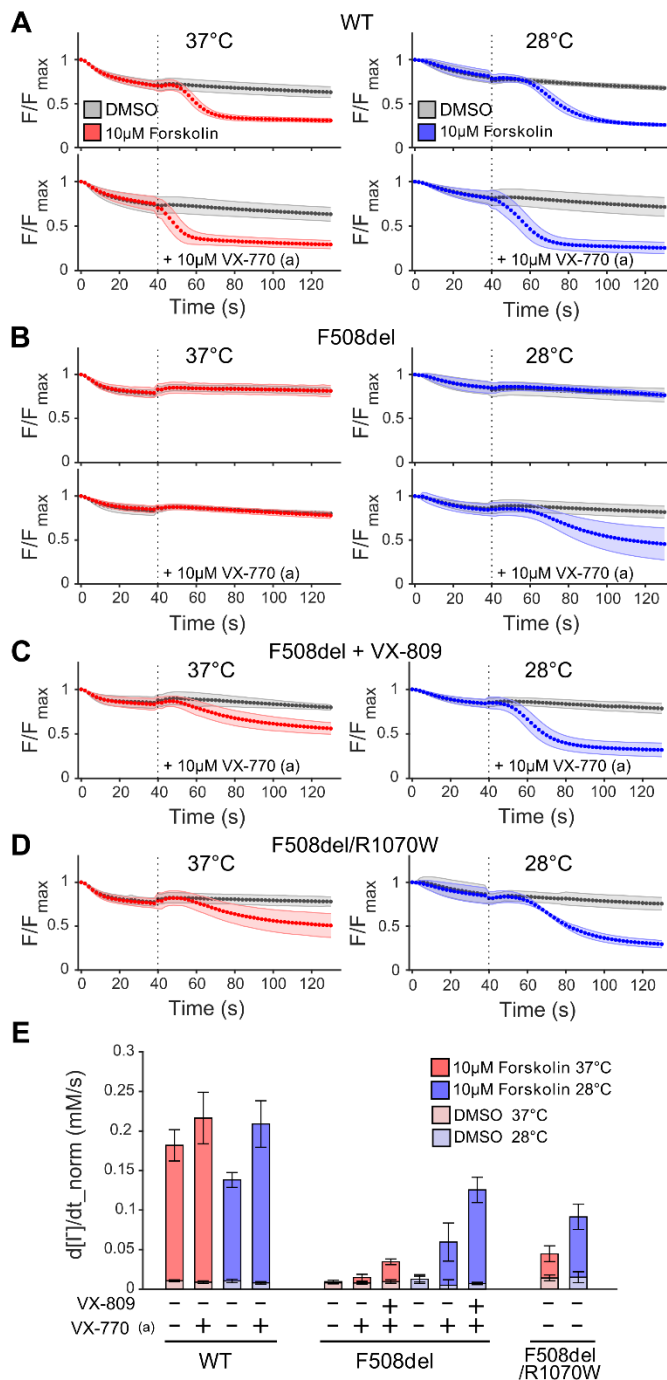
Monitoring CFTR ion channel function. (**A-D**) Quenching of YFP fluorescence in HEK293 cells expressing WT-CFTR (**A**), F508del-CFTR chronically (24 h) treated with DMSO (**B**) or with VX-809 (**C**), and R1070W/F508del-CFTR (**D**). For more information on statistical analysis see Supplementary Tables S2 and S3. Prior to imaging plates were incubated for 24 hours, at 37°C (left panels, red) or 28°C (right panels, blue). This final incubation temperature was maintained throughout image acquisition. At time point 0 s I⁻ was added to the extracellular medium. At 40 s forskolin and, where indicated, VX-770 (acute, a) was added (dotted line),

954   both to a final concentration of 10 µM. The fluorescence before addition of I^- (F_{max}), was used

955   to normalize YFP fluorescence intensity. (**E**) The maximal rate of I^- entry (d[I^-]/dt_norm) is

956   used to summarize CFTR function for genotypes and conditions shown in (**A**-**D**).

34

957 **Figure 4**
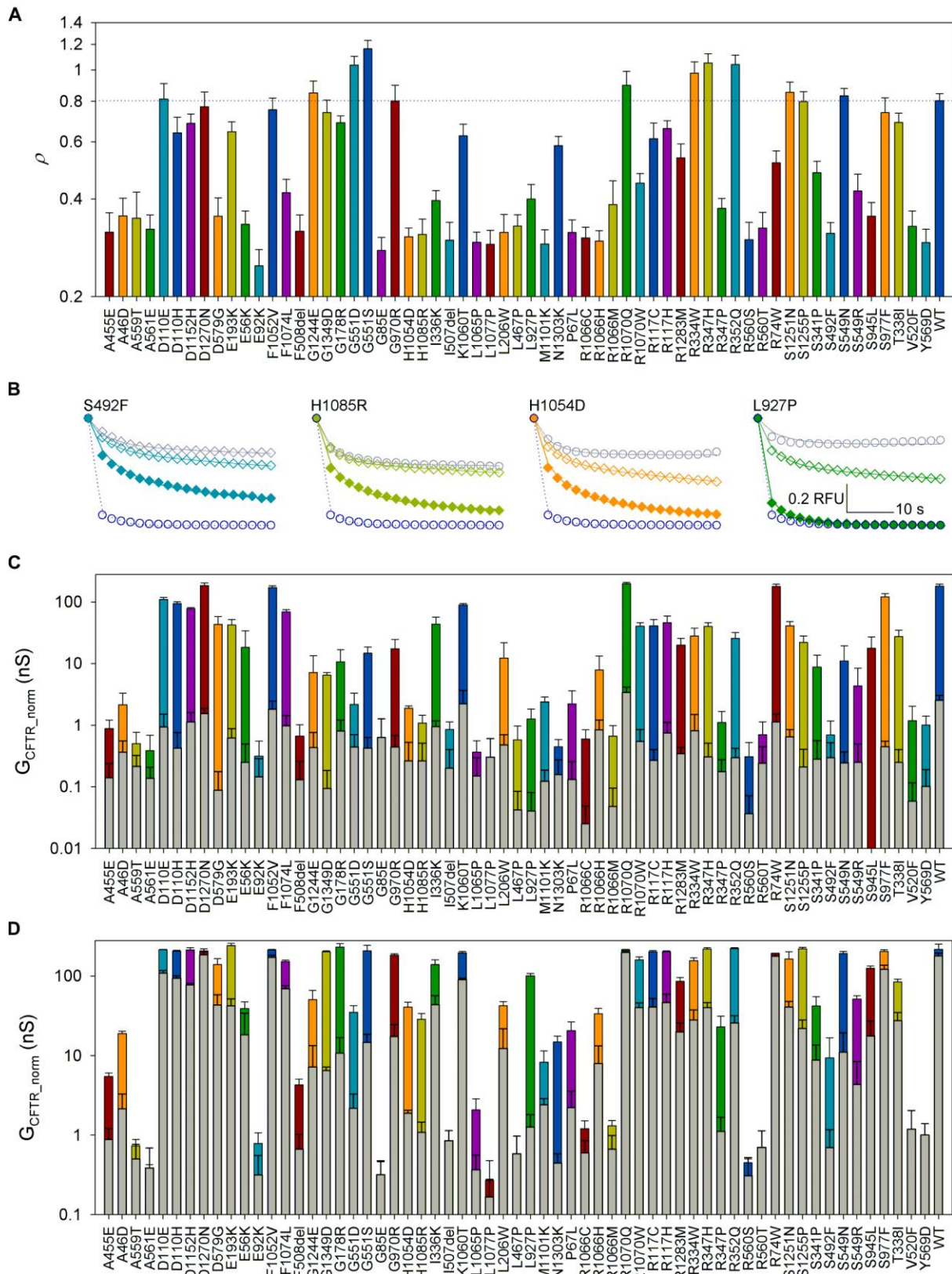
958   Rare CF-mutation profiling. (**A**) Mean ρ (n ≥ 9) of all mutations in the panel. Dotted line

959   indicates mean ρ for WT-CFTR. For ρ distributions, mean ρ and n values for each mutant see

960   Supplementary Figure S5 and Supplementary Table S4. (**B**) Observed YFP quenching time

961   course in the presence of DMSO (grey circles) or 10 µM forskolin (empty coloured diamonds),

962   or 10 µM forskolin + acute 10 µM VX-770 (filled coloured diamonds) for selected mutations.

963   Solid lines show predicted change in proportion of anion-free YFP. For estimated parameters

964   G_{CFTR}, V_M, G_{trans} and τ_{trans} see Supplementary Table S10. WT-CFTR quenching in 10 µM

965   forskolin (dark blue empty circles and dotted line) shown for comparison. (**C**) CFTR

966   conductance of rare mutation panel after activation with 10 µM forskolin (coloured bars) or

967   vehicle control (DMSO, grey bars). n ≥ 3. G_{CFTR} obtained from fitting of quenching time-course

968   for each mutant was normalized using the mean within cell mCherry fluorescence for that

969   mutant, measured with respect to the corresponding metric obtained for WT-CFTR on the same

970   plate. (**D**) Potentiation of rare mutation panel by VX-770. Grey bars show values following

971   activation with 10 µM forskolin alone, coloured bars with further addition of acute 10 µM VX-

972   770. For more information on statistical analysis of quenching data see Supplementary Tables

973   S6 and S7.

974   **Figure 5**
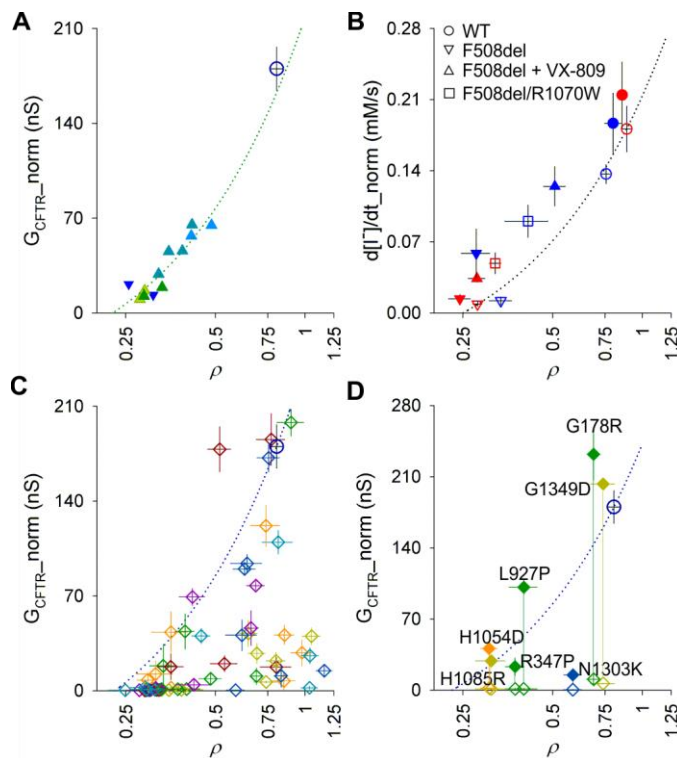
975

976   Investigating permeation/gating characteristics. (**A**) Relationship between normalized CFTR

977   conductance and membrane density in cells expressing F508del-CFTR with no correction (blue

978   ∇) or incubated with increasing concentrations of VX-809 (1 nM to 10 μM, green to light blue

979   Δ), all after activation with 10 μM forskolin and acute potentiation with 10 μM VX-770.

980   F508del-CFTR incubation and measurements were at 28°C. Green dotted line shows linear

981   regression using only F508del-CFTR data points on graph (slope = 281.7, constant = -63.7,

982   resulting in an x-axis intercept at $\rho = 0.23$). Mean value for WT-CFTR activated with 10 μM

983   forskolin alone is shown for reference (from (**C**), large dark blue empty circle). (**B**)

984   Relationship between maximal rate of I⁻ influx and ρ in HEK293 cells expressing WT-CFTR,

985   F508del-CFTR, and F508del/R1070W-CFTR, at 37°C (red symbols) and 28°C (blue symbols).

986   10 μM forskolin was used to activate CFTR. Empty symbols indicate activation with forskolin

987   alone. Solid symbols indicate further acute potentiation with 10 μM VX-770. Dotted line:

988   linear interpolation between data obtained at 37°C for uncorrected F508del-CFTR (used as an

989   empirical measure of minimal membrane density) and WT-CFTR, both without acute VX-770

990   potentiation; slope = 0.284, constant = -0.071, resulting in an x-axis intercept at $\rho = 0.25$. (**C**)

991   Relationship between baseline G_{CFTR_norm} (10 μM forskolin) and ρ for rare mutation panel.

992   Colours as in Figure 4. WT-CFTR is highlighted as a large, dark blue, empty circle. The dark

37

993   blue dotted line (slope = 314.1, constant= -72.3) shows linear interpolation between WT data

994   points and x-axis intercept set at ρ =0.23, as obtained in (**A**). (**D**) Mutants with largest fold

995   potentiation by VX-770 (ratio between conductance obtained in 10 μM forskolin + 10 μM VX-

996   770 over that in 10 μM forskolin alone > 20). Empty diamonds indicate baseline activation

997   with 10 μM forskolin alone, solid diamonds indicate activation following acute potentiation

998   with 10 μM forskolin + 10 μM VX-770.

999 **Figure 6**
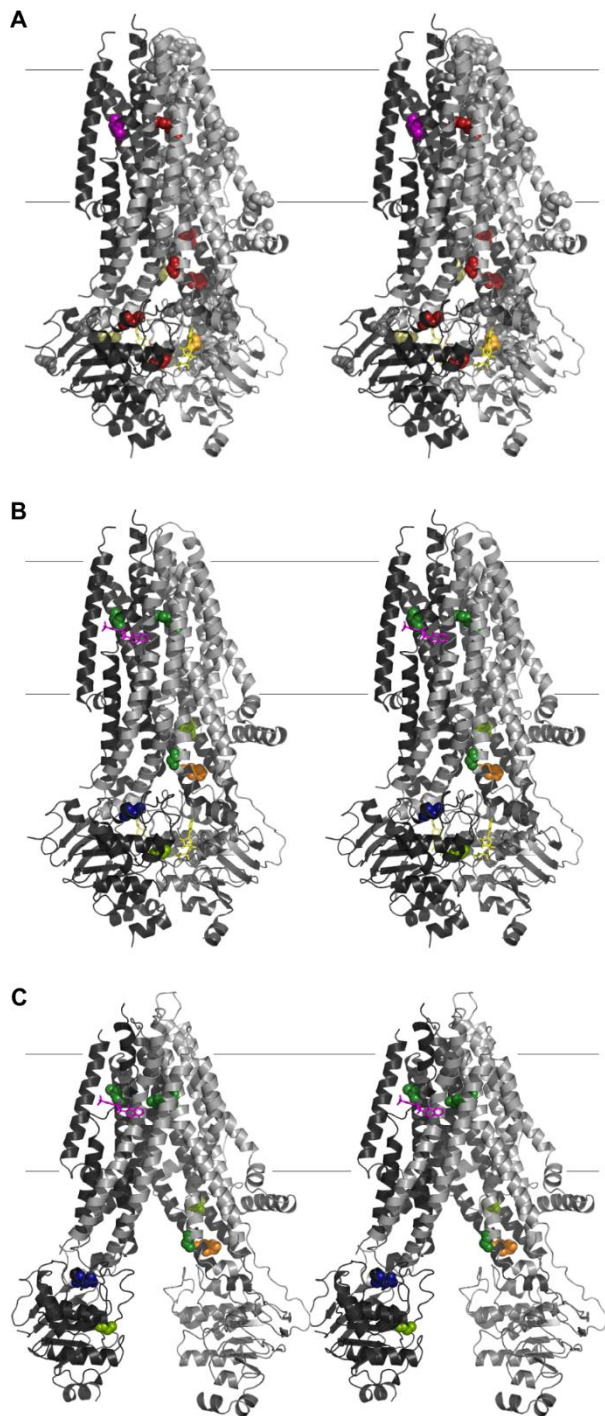
1000

Mapping VX-770 sensitivity on cryo-EM structures. (**A**) Cartoon representation (cross-eye stereo) of phosphorylated, ATP-bound human CFTR, 6MSM (Zhang et al., 2018b), with sites of missense mutations in panel highlighted as spheres. Colours indicate degree of VX-770-potentiaton (fold potentiation, F < 5, grey; 5 < F < 10, white; 10 < F < 15, light yellow; 15 < F < 20, orange; 20 < F < 50, red; F > 50 purple). TMD1-NBD1 in light grey; TMD2-NBD2 in dark grey. Fine horizontal lines show approximate position of membrane boundary. (**B**) Only

1007   positions with most efficacious VX-770 potentiation are shown. Magenta sticks show position

1008   of bound VX-770 in 6O2P structure (Liu et al., 2019). Mutation-site residues are colour-coded

1009   as in Fig. 4 (moving from cytosol to extracellular): G1349, light green; N1303, dark blue;

1010   H1054, orange; G178, forest; H1085, light green; R347, forest right; L927 forest left. (**C**)

1011   Orientation as in (**A,B**) but using atom coordinates of dephosphorylated human CFTR, 5UAK

1012   (Liu et al., 2017).

1013